# Physics in Medicine & Biology

**IPEM**
Institute of Physics and
Engineering in Medicine

**PAPER**

# Characterization of breast tissues in density and effective atomic number basis via spectral X-ray computed tomography

Stevan Vrbaški[1,2,3], Lucia Mariel Arana Peña[1,2,3], Luca Brombal[1,3], Sandro Donato[4,5],
Angelo Taibi[6,7], Adriano Contillo[2] and Renata Longo[1,3]

1 Department of Physics, University of Trieste, Via Valerio 2, I-34127 Trieste, Italy
2 Elettra-Sincrotrone Trieste S.C.p.A, I-34149 Basovizza Trieste, Italy
3 INFN Division of Trieste, Via Valerio 2, I-34127 Trieste, Italy
4 Department of Physics and STAR-Lab, University of Calabria, Via Pietro Bucci, I-87036 Arcavacata, Italy
5 INFN Division of Frascati, Via Enrico Fermi 54, I-00044 Frascati, Italy
6 Department of Physics and Earth Sciences, University of Ferrara, Via Saragat 1, I-44122 Ferrara, Italy
7 INFN Division of Ferrara, Via Saragat 1, I-44122 Ferrara, Italy

**E-mail:** adriano.contillo@elettra.eu

## Abstract

*Objective.* Differentiation of breast tissues is challenging in X-ray imaging because tissues might share similar or even the same linear attenuation coefficients $\mu$. Spectral computed tomography (CT) allows for more quantitative characterization in terms of tissue density ($\rho$) and effective atomic number ($Z_{eff}$) by exploiting the energy dependence of $\mu$. The objective of this study was to examine the potential of $\rho/Z_{eff}$ decomposition in spectral breast CT so as to explore the benefits of tissue characterization and improve the diagnostic accuracy of this emerging 3D imaging technique. *Approach.* In this work, 5 mastectomy samples and a phantom with inserts mimicking breast soft tissues were evaluated in a retrospective study. The samples were imaged at three monochromatic energy levels in the range of 24–38 keV at 5 mGy per scan using a propagation-based phase-contrast setup at SYRMEP beamline at the Italian national synchrotron Elettra. *Main results.* A custom-made algorithm incorporating CT reconstructions of an arbitrary number of spectral energy channels was developed to extract the density and effective atomic number of adipose, fibro-glandular, pure glandular, tumor, and skin from regions selected by a radiologist. *Significance.* Preliminary results suggest that, via spectral CT, it is possible to enhance tissue differentiation. It was found that adipose, fibro-glandular and tumorous tissues have average effective atomic numbers ($5.94 \pm 0.09$, $7.03 \pm 0.012$, and $7.40 \pm 0.10$) and densities ($0.90 \pm 0.02$, $0.96 \pm 0.02$, and $1.07 \pm 0.03$ g cm$^{-3}$) and can be better distinguished if both quantitative values are observed together.

## 1. Introduction

Tissue differentiation in mammography is challenging due to the overlap of tissues with similar linear attenuation coefficients $\mu$ in the diagnostic energy range. A comparison of the attenuation of glandular tissue and close-by malignant tumors found that the average attenuation values are almost identical even in the low-energy range (Chen *et al* 2010, Fredenberg *et al* 2018). Computed tomography (CT) solves tissue overlapping issues and provides additional diagnostic information based on tissue morphology in 3D volumes. On the other hand, breast-dedicated CT uses higher X-ray energies than mammography due to the imaging of uncompressed breasts, thus reducing attenuation contrast between similar tissues. Tissue separation can be significantly improved by acquiring data at multiple energy levels using spectral CT imaging (Alvarez and Macovski 1976). New generations of whole-body spectral CT systems obtain source-generated spectral information from two (or more) scans at different energy levels (dual-energy), or detector-generated spectral response with layered and

photon-counting (PC) detectors. PC detectors are particularly interesting due to the availability of multiple energy thresholds (up to 12 (Danielsson *et al* 2021)), flat spectral response, and low imaging noise. The first breast CT scanners with PC detectors are being introduced in clinics (Kalender *et al* 2017, Berger *et al* 2019, Schmidt *et al* 2022, Zellweger *et al* 2022) and synchrotron facilities (Longo *et al* 2016, 2019), where spectral separation can be obtained using multiple monochromatic x-ray beams. Despite the available technology for spectral imaging in both systems, the benefits of such an approach in breast CT imaging have not been explored yet.

Given two (or more) scans at different energies, the content of each voxel can be described as a linear combination of the attenuation of two basis materials in the process known as material decomposition (Alvarez and Macovski 1976). Decomposition to two basis materials is the most common approach because two physical effects contribute to image formation in the diagnostic energy range: the photoelectric effect and Compton scattering. The photoelectric-Compton basis itself is very convenient because of the well-defined dependencies of these effects on density and atomic number. However, such basis spans an infinite range of physical materials, given that a 'purely Compton' material would be the element in the limit $Z \to 0$, while a 'purely photoelectric' one would correspond to $Z \to \infty$. Such a broad range would degenerate the separation of similar materials, such as soft tissues. To address this issue, the use of a pair of physical (or even virtual) materials that span the range of materials of interest has been shown to significantly reduce decomposition uncertainty (Champley *et al* 2019). A popular choice of physical materials for decomposing biological tissues are polymethyl-methacrylate (PMMA) and aluminum (Al) basis pair (Lehmann *et al* 1981), also used in this study. Estimated weights of the linear combination of two basis materials carry physical information but have no particular comprehensive meaning except when one of the basis materials is the same as the material of interest (e.g. iodine quantification or calcium scoring). However, using the weights and the known energy dependence of basis attenuation coefficients virtual monochromatic images (VMIs) can be extrapolated at an arbitrary energy value within the diagnostic energy range (McCollough *et al* 2015). VMIs have simple interpretation and clinical case studies show that VMIs are diagnostically valuable for certain tasks (Albrecht *et al* 2019), and they are a standard output in the first clinical whole-body PC-CT (Naeotom Alpha, Siemens) (Rajendran *et al* 2021). Decomposition to $\rho$ and $Z_{eff}$ is a step further toward extracting the physical information about tissue composition from spectral measurements. While material decomposition describes the attenuation of one material as a linear combination of the attenuations of other known materials, $\rho/Z_{eff}$ decomposition exploits the underlying physics of x-rays interaction with materials to extract information about their physical and chemical properties. Several works have been published exploring this approach (Heismann *et al* 2003, Torikoshi *et al* 2003, Szczykutowicz *et al* 2011, Azevedo *et al* 2016, Busi *et al* 2019, Champley *et al* 2019, Vrbaski *et al* 2022). Density and $Z_{eff}$ are intuitive units that can be easily interpreted and correspond to physical properties that can be measured by other techniques, allowing for easy comparison. Previous work showed the benefits of $\rho/Z_{eff}$ for tissue differentiation (Pascart *et al* 2019), radiotherapy planning (Hudobivnik *et al* 2016), and interventional radiology (Liu *et al* 2023).

In the present paper, a spectral study was specifically designed to characterize breast CT images in terms of material density $\rho$ and the effective atomic number $Z_{eff}$. While $\rho/Z_{eff}$ decomposition has been implemented in some clinical CT scanners (Rajiah *et al* 2020), no studies specifically focused on breast tissue characterization were performed. In section 2.1, a theoretical approach to computing $\rho$ and $Z_{eff}$ values from physical material decomposition instead of the photoelectric-Compton decomposition was developed to improve the accuracy of results. Using synchrotron x-ray beams at several energies and a high-resolution PC detector described in section 2.2, CT scans of a dedicated phantom and 5 mastectomy samples were acquired. Due to the superior imaging quality and spectral separation available with synchrotron setup, the work investigates the feasibility and the potential diagnostic benefit of $\rho/Z_{eff}$ decomposition in breast CT imaging. This information is of interest since PC detectors matured enough to operate in clinical conditions with the ability to obtain better spectral separation than other approaches mentioned earlier (Danielsson *et al* 2021). The introduced concept of effective atomic number was further investigated in section 2.3 and several approaches to the computation of $Z_{eff}$ were analyzed in appendix C. Section 2.4 describes tissue preparation and section 2.5 provides a detailed explanation of the practical realization of the analysis with careful consideration of the well-known problem of the decomposition noise (Dong *et al* 2014, Niu *et al* 2014, Mechlem *et al* 2016). Finally, the data analysis approach is given in section 2.6. We also showed that virtual monochromatic $\mu$ values at desired energy can be computed using the known dependence of x-ray attenuation on density and atomic number.

## 2. Materials and methods

### 2.1. Theoretical model

In the material decomposition approach, the attenuation coefficient $\mu$ of a given material is expressed as a linear combination of the (known) attenuation coefficients of a pair of basis materials, here labeled $\mu_1$ and $\mu_2$

$$\mu = x_1\,\mu_1 + x_2\,\mu_2, \tag{1}$$

where $x_1$ and $x_2$ are the coordinates of the material in the reference frame identified by the selected basis. In the first step of our method, we used equation (1) to determine the coefficients $x_1$ and $x_2$, which represent the (energy-independent) relative concentrations of each basis material. Because more than two spectral scans were available for each sample (Piai *et al* 2019), instead of using traditional matrix inversion (Zhang *et al* 2019), $x_1$ and $x_2$ coefficients were calculated by using a least-square fit of the form:

$$\sum_i (\mu(E_i) - (x_1\,\mu_1(E_i) + x_2\,\mu_2(E_i)))^2. \tag{2}$$

The fit procedure consists of a voxel-by-voxel minimization of the sum over the energies $E_i$ of the squared residuals. From such a point of view, including more images of different energies adds further points to the plane, which is expected to increase the accuracy of the decomposition.

The attenuation of X-rays is influenced by several physical effects, which are dependent on the energy and material properties of the attenuator. In the range of photon energies useful for medical CT imaging, the attenuation coefficient $\mu$ of given material of density $\rho$, the atomic number $Z$, and atomic mass $A$ are approximated as the sum of the two contributions

$$\mu(\rho, Z, A, E) = \frac{\rho\,Z}{A}[K_1\,Z^{n-1}\,f_P(E) + K_2\,f_C(E)], \tag{3}$$

where the functions $f_P(E)$ and $f_C(E)$ encode the energy dependencies of the photoelectric and Compton effects, respectively, and $K_1$, $K_2$ and $n$ are constants. Using equation (3) to describe basis materials in equation (1) and assuming $A = 2Z$, as it is almost true for any chemical element with $Z \lesssim 20$, the linear combination coefficients of equation (1) read

$$x_1 = \frac{\rho\,Z_1(Z^n Z_2 - Z\,Z_2^n)}{\rho_1 Z(Z_1^n Z_2 - Z_1 Z_2^n)}, \tag{4a}$$

$$x_2 = \frac{\rho\,Z_2(Z\,Z_1^n - Z^n Z_1)}{\rho_2 Z(Z_1^n Z_2 - Z_1 Z_2^n)} \tag{4b}$$

$\rho_j$ and $Z_j$ being the density and the atomic number of the $j$th basis material. It is straightforward to notice that equations (4a) and (4b) depend on both the density and the atomic number of the material. In order to decouple the two dependencies, it is necessary to rotate the reference frame (by an angle $\phi = \arctan(\rho_2/\rho_1)$) and then rescale the second coordinate dividing it by the first one. The resulting coordinates, which read

$$x_\rho = \frac{\rho}{\sqrt{\rho_1^2 + \rho_2^2}}, \tag{5a}$$

$$x_Z = \frac{Z^\ell(\rho_1^2 + \rho_2^2) - (Z_1^\ell\,\rho_1^2 + Z_2^\ell\,\rho_2^2)}{(Z_2^\ell - Z_1^\ell)\rho_1\rho_2} \tag{5b}$$

(with $\ell = n - 1$) are labeled $x_\rho$ and $x_Z$ because of their exclusive dependencies on the variables mentioned in the subscripts. Equations (5a) and (5b) represent the expected relationships between $x_\rho$ and $\rho$, and between $x_Z$ and $Z$, for a given choice of basis materials. Such expressions are used in the calibration procedure described in section 3.1, where the (known) densities and atomic numbers of reference materials will be fitted against the corresponding (measured) values of $x_\rho$ and $x_Z$ using the functional forms

$$x_\rho(\rho) = \kappa\,\rho, \tag{6a}$$

$$x_Z(Z) = p\,Z^\lambda + q \tag{6b}$$

stemming directly from equations (5a) and (5b) with the (physically motivated) coefficients replaced by the effective fit parameters $\kappa$, $\lambda$, $p$, and $q$. The resulting calibrated relationships map the measured $x_\rho$ and $x_Z$ of any imaged material onto its actual values of density and effective atomic number.

## 2.2. Scan setup

The experimental image acquisition was carried out at the SYRMEP beamline of Elettra, an Italian synchrotron light source in Trieste, in the framework of SYRMA-3D (SYnchrotron Radiation for MAmmography) collaboration (Longo *et al* 2019). The SYRMEP beamline utilizes a laminar beam having a cross-section at the detector equal to 148.5 mm (horizontal) $\times$ 3.25 mm (vertical), while the energy is selected through a Si double-crystal (1, 1, 1) monochromator with a resolution around 0.1%. To perform tomographic acquisition the sample was positioned on a rotation stage spinning at a constant speed of 4.5 degrees s$^{-1}$ while 1200 projections were acquired over 180 degrees. The imaging detector was a large area high-resolution CdTe PC device (Pixirad8) featuring a honeycomb matrix of 4096 $\times$ 476 pixels with a 60 $\mu$m horizontal and 52 $\mu$m vertical pitch (Bellazzini *et al* 2013, Delogu *et al* 2016). It was positioned $\sim$1.6 m from the sample to employ the propagation-based phase-

**Table 1.** List of materials composing the phantom together with chemical formulas, effective atomic numbers, and material density values (Schoonjans *et al* 2011).

| Material | Water | PE | PA | PMMA | POM | PTFE |
|---|---|---|---|---|---|---|
| Brute formula | $H_2O$ | $C_2H_4$ | $C_{12}H_{22}N_2O_2$ | $C_5H_8O_2$ | $CH_2O$ | $C_2F_4$ |
| Effective $Z$ | 7.44 | 5.28 | 6.16 | 6.49 | 7.01 | 8.56 |
| Density (g cm$^{-3}$) | 1.0 | 0.94 | 1.14 | 1.19 | 1.425 | 2.2 |

contrast imaging technique. The source-to-sample distance was 30 m, leading to a magnification factor of 1.05. Acquired projections were pre-processed with an ad-hoc procedure (Brombal *et al* 2018a) and then phase-retrieved using an algorithm based on the homogeneous transport of intensity equation (TIE-Hom) (Paganin *et al* 2002). Finally, CT reconstructions were obtained via a GPU-based filtered-back-projection algorithm with Shepp-Logan filtering (Brun *et al* 2017). It is worth noting that, despite being a product of phase retrieval, reconstructions are maps of the attenuation coefficients $\mu$ at a given energy, as thoroughly explained in Gureyev *et al* (2017), Brombal *et al* (2018b), Piai *et al* (2019).

### 2.3. Calibration phantom and effective atomic number
A custom-made cylindrical phantom with a 10 cm diameter dedicated to calibration and quality control of the synchrotron breast CT system was used (Contillo *et al* 2018, Donato *et al* 2022). The phantom was filled with water and contained five inserts of polyethylene (PE), nylon (PA), PMMA, polyoxymethylene (POM), and polytetrafluoroethylene (PTFE) mimicking soft tissues of similar attenuation properties. The density of these materials and material composition used to compute effective atomic numbers were taken from the xraylib database (Brunetti *et al* 2004). The atomic number is a physical property of an element, but the same concept cannot be trivially defined in compounds. Across the literature (Spiers 1946, Tsai and Cho 1976, Puumalainen *et al* 1977, Un and Caner 2014, Azevedo *et al* 2016, Champley *et al* 2019) several definitions have been proposed, suggesting that it depends not just on material properties, but also experimental conditions (Bonnin *et al* 2014). We included most of the published definitions in the open-source GUI software 'Z*comp*ARE' (Vrbaski 2022). Part of the software is built on top of the Python library (xraylib 4.1.0 package, Python 3.10) of the xraylib database (Brunetti *et al* 2004, Schoonjans *et al* 2011) and can be used to compare approaches for computing atomic numbers of compounds from this database or list of user-defined materials can be provided. A comparison between the methods using this software is analyzed in appendix B, showing that depending on the method chosen, $Z_{eff}$ number can take different values for the same compound. However, any choice of the method led to a unique material description in chosen basis. Quantity $x_Z$ derived in section 2.1, was simply calibrated to the desired definition of effective atomic number for a compound by putting $Z = Z_{eff}$ in equation (6*b*). In this paper, we used the approach by Champley *et al* (2019) which defines $Z_{eff}$ of a compound as a linear combination of two consecutive $Z$ numbers such that the least square error between x-ray transmission of the compound and the transmission of a combination of the two elements is minimized. Compounds' brute formula, density, and $Z_{eff}$ are given in table 1. The phantom served two purposes: (i) to obtain the $\rho$ and $Z_{eff}$ calibration curve from the decoupled set in equations (5*a*) and (5*b*) and (ii) to validate the theoretical model against the ground truth.

### 2.4. Breast mastectomy samples
In addition to phantom scanning, post-mastectomy breast tissue images were analyzed in a retrospective study. The analyzed surgical samples ($N = 5$) were fixed in formalin, sealed in a vacuum bag, and conserved at 4 °C. The preliminary analysis of the same data was published (Piai *et al* 2019) as a feasibility study of the synchrotron breast CT approach. All the procedures adopted in this work followed Directive 2004/23/EC of the European Parliament and of the Council of 31 March 2004 on setting standards of quality and safety for the donation, procurement, testing, processing, preservation, storage, and distribution of human tissues. In the present work, we further processed the data to extract $\rho$ and $Z_{eff}$ of breast tissues. Tomographic reconstructions of selected samples are given in figure 1. They all contained adipose, fibro-glandular, and tumorous tissue, but only in sample 4 existed a region of glandular tissue clearly separated from the fibrous. It also contained calcification regions that were not evaluated in this study. All samples contained some type of malignant tissue: samples 1, 2, and 3 contain infiltrating ductal carcinoma, sample 4 contains infiltrating ductal carcinoma with a core of desmoplastic tissue, and sample 5 contains vastly differentiated infiltrating ductal carcinoma. Samples 1, 2, 4, and 5 also contained portions of the skin.

The mean glandular dose of 5 mGy delivered per scan was computed according to a dedicated Geant4 Monte Carlo simulation (Fedon *et al* 2015, Mettivier *et al* 2016). The phantom scans were acquired at 25, 28, 32, and
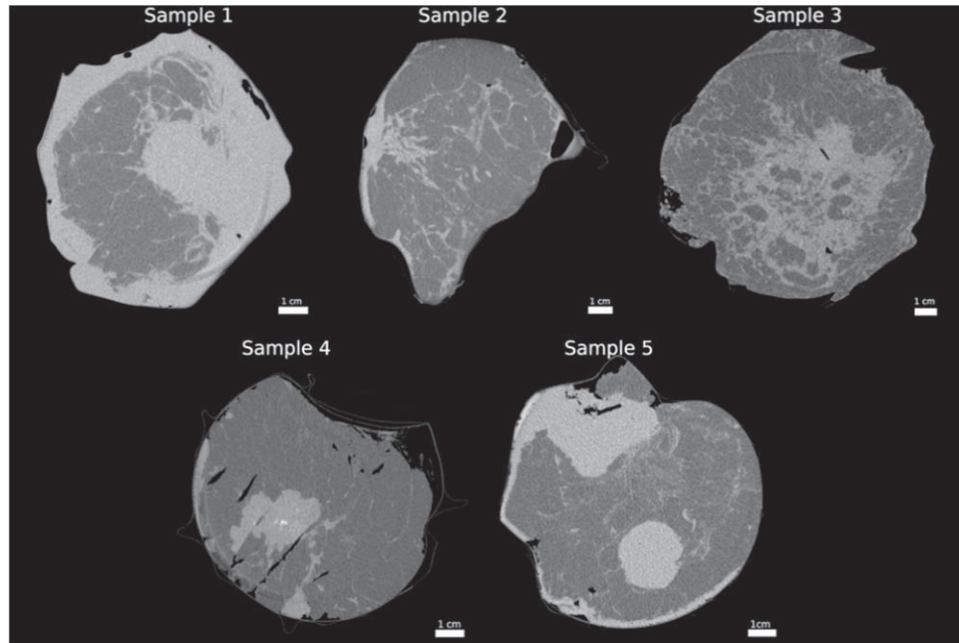
**Figure 1.** Mastectomy CT reconstructions acquired at SYRMEP beamline at Elettra Sincrotrone Trieste at the energy of 28 keV (sample 1, 2, 3, and 5) and 26 keV (sample 4).

35 keV, and mastectomy samples at several monochromatic beam energy levels in the range of 24–38 keV, from which three scans were selected for the spectral analysis.

### 2.5. Practical implementation

The theoretical model described in section 2.1 was implemented with Python (Python 3.10.0) and an interactive delineation tool was developed to select an arbitrary region of interest within a reconstructed spectral data set (Matplotlib, Python 3.10.0) containing a single tissue type. In the first step of the process (framed with a dashed line in figure 2), the voxel-to-voxel material decomposition method using the PMMA-Al basis is applied to the selected regions (figure 2(a)), resulting in PMMA and Al maps for each ROI (figure 2(b)). In the next step, the material maps are combined into 2D histograms, one for each tissue type (figure 2(c)). In literature, this approach to material visualization is often referred to as CT fingerprinting (Rajiah *et al* 2020). Due to the presence of noise, the obtained histograms are blurred and elongated.

The correct decomposition coefficients $x_1$ and $x_2$ are considered to be the centers of obtained distributions. They are extracted using a 2D Gaussian fit method of the form:

$$G(x_1,\, x_2) = A\; e^{\left(-\frac{u^2}{2\,s_u^2} + \frac{v^2}{2\,s_v^2}\right)} \tag{7}$$

$A$ is the intensity of the peak and $S_u$, $S_v$ the spreads (that is, the standard deviations of the associated distributions) along the major and minor axes, respectively. The peak coordinates $\bar{x}_1$ and $\bar{x}_2$ relative to $(x_1, x_2)$-plane of the histogram are contained in the quantities $u$ and $v$
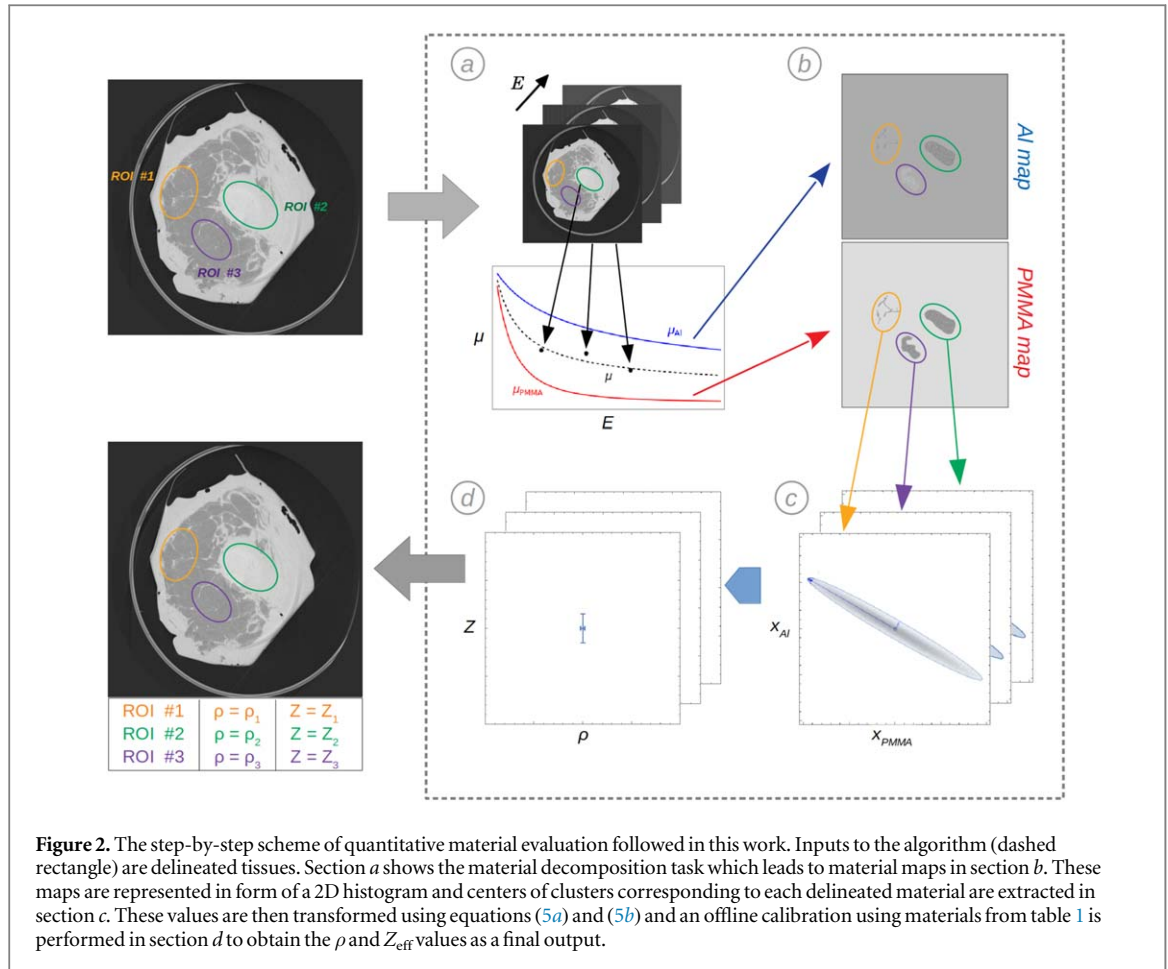
$$u = (x_1 - \bar{x}_1)\cos\theta + (x_2 - \bar{x}_2)\sin\theta, \tag{8a}$$

$$v = (x_2 - \bar{x}_2)\cos\theta - (x_1 - \bar{x}_1)\sin\theta \tag{8b}$$

$\theta$ is the tilt of the major axis of the spot with respect to the horizontal direction. After the fitting, the peak coordinates $\bar{x}_1$ and $\bar{x}_2$ found according to equations (8a) and (8b) are used in equations (4a) and (4b) to compute the final output of the procedure: the single values for densities and effective atomic numbers of selected tissues (figure 2(d)). The measurement uncertainty, estimated as the standard error on the center of fitted 2D Gaussian distribution, is propagated through all mathematical transformation steps and measurement calibration. For the sake of conciseness, the complete analysis is given in appendix A.

### 2.6. Data analysis

In addition to the experimental data obtained using the calibration phantom, the procedure described in the theoretical model (section 2.1) was also applied to published $\mu$ ('true') values (Schoonjans *et al* 2011) of phantom material inserts at the energy levels used in the experiment. The true data points are used to evaluate the accuracy of the model by calculating the percentage error between the experimental and the ground truth data points, as

**Figure 2.** The step-by-step scheme of quantitative material evaluation followed in this work. Inputs to the algorithm (dashed rectangle) are delineated tissues. Section *a* shows the material decomposition task which leads to material maps in section *b*. These maps are represented in form of a 2D histogram and centers of clusters corresponding to each delineated material are extracted in section *c*. These values are then transformed using equations (5*a*) and (5*b*) and an offline calibration using materials from table 1 is performed in section *d* to obtain the $\rho$ and $Z_{\text{eff}}$ values as a final output.

given in equation (9)
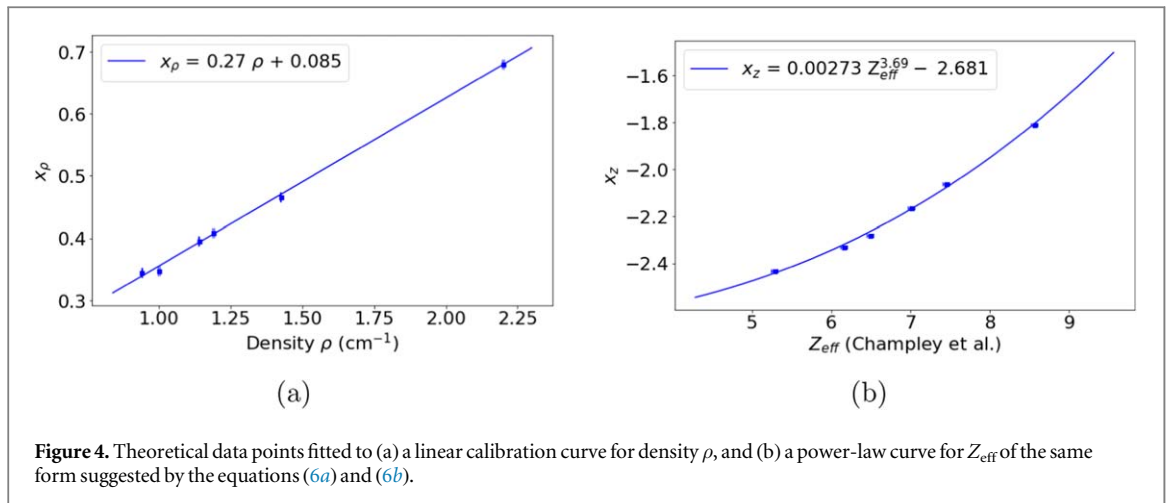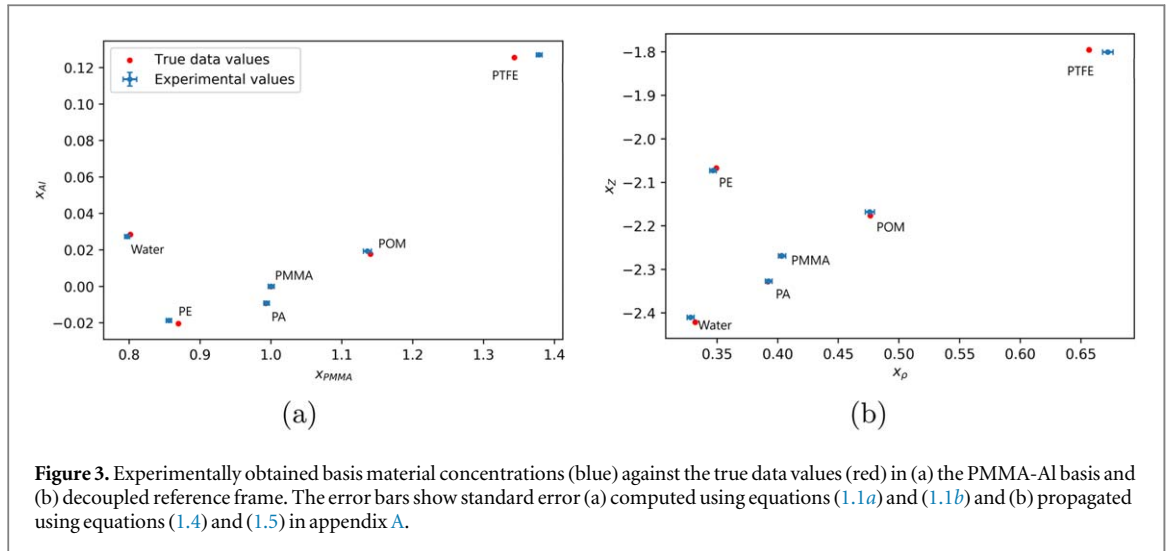
$$\% \ error = \frac{|\text{ground truth} - \text{measured}|}{\text{ground truth}} \times \ 100. \tag{9}$$

The segmentation of the breast CT reconstructions was performed by an experienced radiologist, who selected ROIs containing adipose, fibro-glandular, glandular, skin, and tumorous tissue already knowing the mastectomy content from specimens sampled for the histological examination. Considering magnification, slices were reconstructed with $0.057 \times 0.057$ mm pixel size and slice thickness of 0.049 mm. The segmentation was done slice by slice to extract values from a 3D volume, using at least 3 pixel thick (0.17 mm) margins to avoid partial volume effects. For each sample and tissue type, density and $Z_{\text{eff}}$ values and their uncertainties were estimated respectively as the mean and standard deviation evaluated over 10 consecutive CT slices. To estimate the discrimination power of $\rho/Z_{\text{eff}}$ and $x_{\text{PMMA}}$ and $x_{\text{Al}}$ decomposition, hence diagnostic potential, a mean Silhouette score (MSS) using Euclidean distance as a metric was computed on mean values of all tissue types collected from the mastectomy samples (Rousseeuw 1987). The MSS is a tool to quantify how similar are samples within the same cluster and how separated they are from other clusters, defined as:

$$\text{MSS} = \frac{1}{n}\sum_{k=0}^{n} \frac{\text{NC}_k - \text{IC}_k}{max(\text{NC}_k,\ \text{IC}_k)}, \tag{10}$$

where IC is the mean intra-cluster distance and NC is the mean nearest-cluster distance for each sample $k$, and $n$ equals the number of selected tissue types $\times$ number of selected mastectomy samples. Negative values of MSS indicate cluster overlap, values around 0 signal that samples are on or close to the boundary between clusters, and positive values up to 1 indicate increased cluster separation.

Finally, extracted density and effective atomic numbers from the calibration phantom and sample 4 were fed to the mathematical relationship given in equation (3) to extrapolate linear attenuation coefficients of tissues for arbitrary (virtual) monochromatic energy levels. The uncertainty was propagated from the standard deviation of obtained $\rho$ and $Z_{\text{eff}}$ values.

**Figure 3.** Experimentally obtained basis material concentrations (blue) against the true data values (red) in (a) the PMMA-Al basis and (b) decoupled reference frame. The error bars show standard error (a) computed using equations (1.1*a*) and (1.1*b*) and (b) propagated using equations (1.4) and (1.5) in appendix A.



**Figure 4.** Theoretical data points fitted to (a) a linear calibration curve for density $\rho$, and (b) a power-law curve for $Z_{eff}$ of the same form suggested by the equations (6*a*) and (6*b*).

## 3. Results

### 3.1. Calibration phantom results

The accuracy of material decomposition in phantom materials following the Gaussian fitting in the histogram space is shown in figure 3(a). Quantities $x_1$ and $x_2$ in equations (4*a*) and (4*b*) are replaced with $x_{PMMA}$ and $x_{Al}$ because of the particular basis choice. Figure 3(b) corresponds to the decoupling of density and effective atomic number in equations (5*a*) and (5*b*). The fitting parameters $A$, $S_u$, $S_v$ defined in equation (7), and angle $\theta$ for phantom materials are given and further discussed in appendix B.

The decoupled values from figure 3(b) were calibrated to absolute density and effective atomic numbers (table 1) applying the least-squares fitting method to the functional forms given in equations (6*a*) and (6*b*). Both calibration curves were based on the phantom material inserts in the range of interest for soft tissue imaging and the mapping to correct density and the effective atomic number was obtained at $R^2 = 0.998$ and $R^2 = 0.997$, respectively. Calibration curves are given in figure 4 and corresponding density and $Z_{eff}$ values are given in table 2. Using equation (9), % errors in calibration materials were estimated to be below 3% and 1.5%, respectively, after the density and effective atomic number calibration.

### 3.2. Breast mastectomy results

Tissues inside the mastectomies delineated by a radiologist were quantitatively analyzed in terms of their density and effective atomic number and presented in figure 5, with average values given in table 3. For comparison, decomposition to basis material coefficients $x_{PMMA}$ and $x_{Al}$ are also given in figure 5. Skin tissue was not included in the graph as it is anatomically well separated from other tissues of the breast.

The level of separation between adipose, fibro-glandular, and tumor tissue in $\rho$ and $Z_{eff}$ space was found to be 0.31 (on a scale of $-1$ to 1) using MSS. Pairwise comparison of adipose and fibro-glandular (MSS = 0.59),
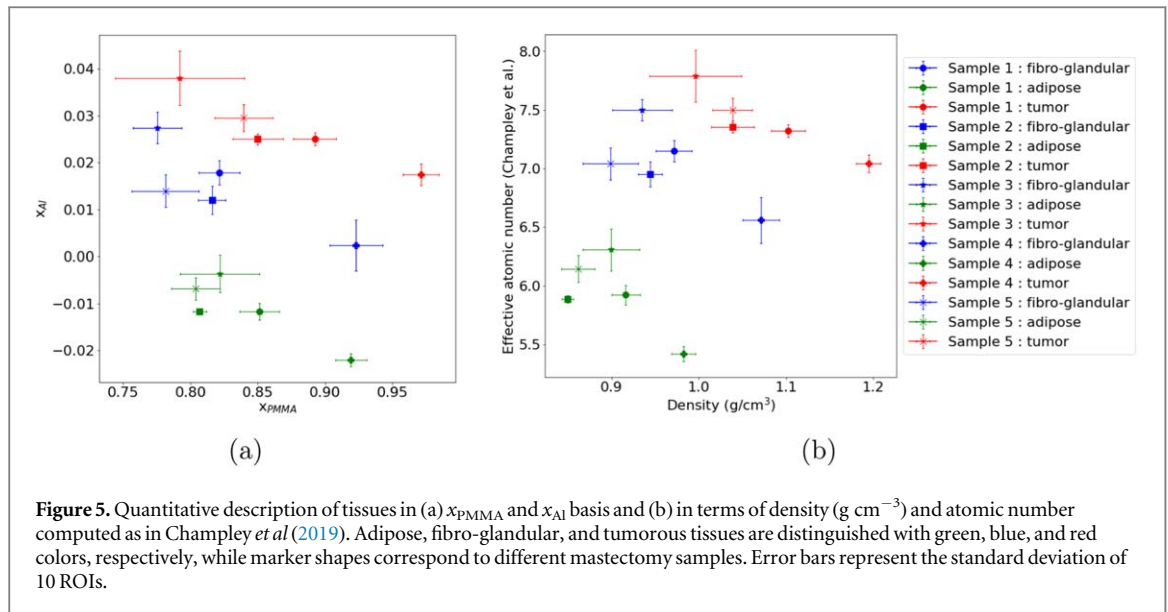
**Figure 5.** Quantitative description of tissues in (a) $x_{PMMA}$ and $x_{Al}$ basis and (b) in terms of density (g cm$^{-3}$) and atomic number computed as in Champley *et al* (2019). Adipose, fibro-glandular, and tumorous tissues are distinguished with green, blue, and red colors, respectively, while marker shapes correspond to different mastectomy samples. Error bars represent the standard deviation of 10 ROIs.

**Table 2.** $Z_{eff}$ and $\rho$ with the corresponding standard errors $\sigma_Z$ and $\sigma_\rho$ obtained from the calibration phantom and %*err* computed using equation (9).

| Material | $\rho \pm \sigma_\rho$ (g cm$^{-3}$) | $Z_{eff} \pm \sigma_{Z_{eff}}$ | %*err* $\rho$ | %*err* $Z_{eff}$ |
|---|---|---|---|---|
| PE | $0.963 \pm 0.004$ | $5.36 \pm 0.02$ | 2.4 | 1.3 |
| Water | $0.971 \pm 0.001$ | $7.51 \pm 0.02$ | 2.9 | 0.9 |
| PA | $1.149 \pm 0.004$ | $6.10 \pm 0.01$ | 0.7 | 1.0 |
| PMMA | $1.198 \pm 0.004$ | $6.40 \pm 0.01$ | 0.7 | 1.4 |
| POM | $1.411 \pm 0.004$ | $7.04 \pm 0.01$ | 1.0 | 0.4 |
| PTFE | $2.204 \pm 0.003$ | $8.55 \pm 0.01$ | 0.2 | 0.2 |

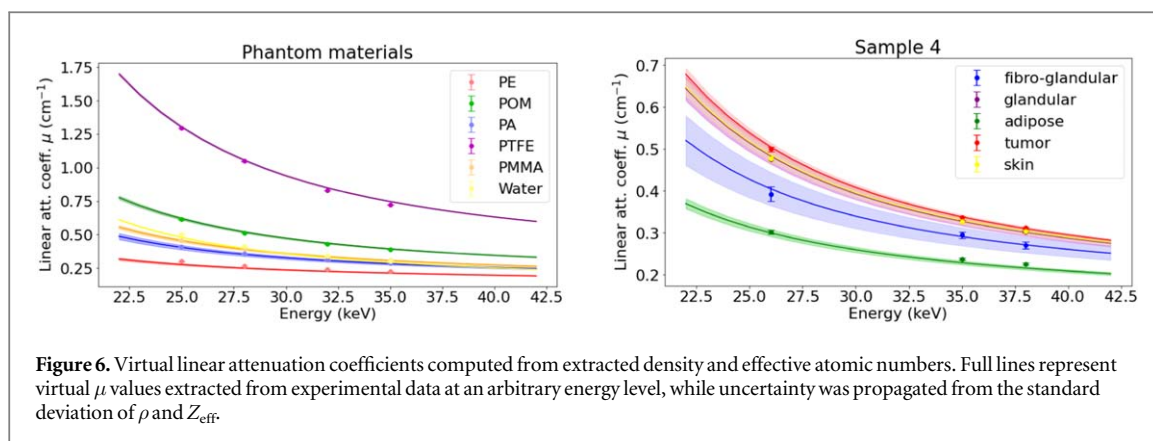**Table 3.** Average $Z_{eff}$ and $\rho$ from 5 mastectomy samples.

| Tissue type | $\rho \pm SD_\rho$ (g cm$^{-3}$) | $Z_{eff} \pm SD_{Z_{eff}}$ |
|---|---|---|
| Adipose | $0.90 \pm 0.02$ | $5.94 \pm 0.09$ |
| Fibro-glandular | $0.96 \pm 0.02$ | $7.03 \pm 0.12$ |
| Tumor | $1.07 \pm 0.03$ | $7.40 \pm 0.10$ |
| Skin | $1.08 \pm 0.02$ | $7.31 \pm 0.06$ |

adipose and tumor (MSS = 0.74), and fibro-glandular and tumor (MSS = 0.17) showed that adipose tissue can be distinguished from the other two, while fibro-glandular and tumor are closer together in $\rho/Z_{eff}$ space. In comparison, MSS in $x_{PMMA}$ and $x_{Al}$ space was $-0.02$. From figure 5 it can be seen that adipose tissue can be distinguished from fibro-glandular and tumorous purely based on effective atomic number values. On the other hand, fibro-glandular and tumorous tissues are overlapping both in their effective atomic numbers and densities and can be distinguished only if both quantitative values are observed together.

In addition to adipose, fibro-glandular, and malignant tissue, the mastectomy labeled as sample 4 contains well-separated pure glandular tissue and skin. Thus, an extensive investigation was conducted on this tissue. Extracted density and effective atomic number were $0.98 \pm 0.01$ and $5.42 \pm 0.06$ for adipose, $1.07 \pm 0.02$ and $6.56 \pm 0.20$ for fibro-glandular, $1.18 \pm 0.02$ and $6.88 \pm 0.09$ for glandular, $1.19 \pm 0.01$ and $7.04 \pm 0.07$ for tumorous, and $1.19 \pm 0.02$ and $6.87 \pm 0.04$ for skin tissue, respectively. In this particular mastectomy sample, mean density and $Z_{eff}$ are not distinguishable between the skin and glandular tissue. Glandular tissue has higher $Z_{eff}$ and density than fibro-glandular tissue, but almost the same density and slightly lower $Z_{eff}$ than tumorous tissue.

Virtual $\mu$ values of phantom materials and tissues in sample 4 are given in figure 6. The obtained $\rho$ and $Z_{eff}$ values correctly map to experimentally measured $\mu$ values and provide information about tissue separation at lower energies with respect to those used for tissue scanning.

**Figure 6.** Virtual linear attenuation coefficients computed from extracted density and effective atomic numbers. Full lines represent virtual $\mu$ values extracted from experimental data at an arbitrary energy level, while uncertainty was propagated from the standard deviation of $\rho$ and $Z_{\mathrm{eff}}$.

# 4. Discussion

Conventional CT scans offer a relatively low specificity when distinguishing between soft tissues of slightly different compositions. On the other hand, spectral imaging advances the ability to distinguish such tissues by probing their attenuation properties at several energy levels. Spectral information is used for the decomposition of data in basis materials, such as PMMA-Al. The decomposed material maps can be used as an intermediate step to estimating the uniquely defined physical quantities of imaged tissues. Utilizing these quantities, virtual monochromatic $\mu$ values at arbitrary energy levels can be further extrapolated. In this work, a new approach to material decomposition and $\rho/Z_{\mathrm{eff}}$ estimation was presented to characterize breast tissues.

A least-square fitting approach to two-basis material decomposition was adopted for an over-determined system when $\mu$ values can be measured at several energy levels. This was the case in our retrospective study with monochromatic beams, but the same approach can be applied to multi-threshold photon counting detectors. The procedure for decoupling density from $Z_{\mathrm{eff}}$ depends on the quality of performed material decomposition, but is at the same time independent of the method itself, and can be applied to other methods published in the literature. Experimentally computed concentrations $x_{\mathrm{PMMA}}$ and $x_{\mathrm{Al}}$ of basis materials and related basis $x_\rho$ and $x_Z$ in the phantom were found to be in good agreement with the ground truth values. Moreover, small associated standard errors in figure 3 show that plastic inserts can be separated in both material and $x_\rho/x_Z$ basis. The theoretically derived functions in equations (6*a*) and (6*b*) were fitted to 6 data points corresponding to tissue-equivalent plastics in the phantom. The high accuracy ($R^2 > 0.99$) of the fitting procedure justifies the assumptions made in theoretical derivation. The systematic errors observed in figure 3 for some materials (e.g. PTFE and PE), which can probably be ascribed to slight differences between the composition of the phantom materials and the ones published in Schoonjans *et al* (2011), do not impact the process of calibration, leading to an agreement with the ground truth data at an average % error of 1.34% for $\rho$ and 0.89% for $Z_{\mathrm{eff}}$, as shown in table 2. These results demonstrate that soft-tissue-equivalent plastic materials of similar composition can be distinguished from spectral CT data using estimated effective atomic number and density values.

The preliminary study on the breast cancer mastectomy samples was an attempt to demonstrate the feasibility of our method to distinguish between fibro-glandular and tumorous tissues inside the breast. Based on the available samples, it was shown that starting from spectral data it is possible to separate adipose, fibro-glandular and tumorous tissues based on their physical characteristics. This might be useful in risk assessment, cancer diagnosis, and the assessment of the status of the disease. Although pure glandular and tumorous tissue in Sample 4 had almost the same density and slightly different effective atomic numbers, this could be due to the desmoplastic core present inside the tumor and no conclusions could be made based on a single piece of evidence. The importance of $Z_{\mathrm{eff}}$ to x-ray attenuation can be observed when comparing adipose and fibro-glandular tissue clusters. It can be seen that lower $\mu$ values for adipose tissue are driven by lower $Z_{\mathrm{eff}}$, rather than significantly lower density. Distinguishing tumorous and pure glandular tissue is challenging because only slight differences exist in both density and $Z_{\mathrm{eff}}$. In our study, we observed that it is not possible to distinguish between different tissues solely on density or effective atomic number or $\mu$ value alone while reasonable discrimination (MSS = 0.31) can be obtained considering 2D clusters in $\rho/Z_{\mathrm{eff}}$ space. A worse separation (MSS = $-0.02$) can be obtained using just material coefficients $x_{\mathrm{PMMA}}$ and $x_{\mathrm{Al}}$. Therefore, using density and effective atomic number maps in the diagnostic workflow could be beneficial, potentially allowing the identification of the tissue type based on quantitative measurements. Because of improved tissue separation, interpretability, as well as the ability to measure these quantities with other experimental techniques, density and $Z_{\mathrm{eff}}$ should be preferred over a simple material decomposition approach.

VMIs are usually computed directly from decomposed basis (e.g. $\mu_1$ and $\mu_2$) using $x_1$ and $x_2$ in equation (1). Equivalently, physically relevant $\rho/Z_{eff}$ space can be used to compute other quantitative maps established in clinical practice. Linear attenuation values in figure 6 were calculated using equation (3) at energies within and outside the energy range used in the experiment. Virtual $\mu$ values calculated using the $Z_{eff}$ defined by Champley *et al* (2019) were in agreement (within the measurement error) with experimentally measured $\mu$ coefficients in both the phantom and sample 4 and they enabled comparison with experimentally obtained $\mu$ values in other studies. For sample 4, which contained tissues examined by Fredenberg *et al* (2018), $\mu$ values were compared at energies of 20, 30, and 40 keV with an average % error of 3.3, 7.3, and 3.4%, for glandular, adipose, and tumor tissue, respectively.

Our approach to tissue analysis could be directly applied to state-of-the-art synchrotron radiation breast CT setups currently developed in Trieste at Elettra Sincrotrone SYRMEP beamline (Longo *et al* 2019), and at ANSTO Imaging and Medical beamline in Australia (Tavakoli Taba *et al* 2021). With these experimental settings, it should be mentioned that multiple energy acquisitions would be required, thus resulting in an increased dose to the breast. On the other hand, due to the high contrast-to-noise ratio of phase-contrast images, the dose per scan could be reduced thus bringing overall acceptable radiation exposures. Considering clinical systems in hospitals, the advent of spectral CT paves the way to material decomposition following a single shot acquisition without a significant increment of the dose. Photon-counting breast CT systems are in clinical practice (Berger *et al* 2019) and an extension to spectral applications is expected.

Studies estimating both $\rho$ and $Z_{eff}$ of human tissues using synchrotron CT systems are almost nonexistent. The study by Torikoshi *et al* (2003) introduced a method to compute these quantities avoiding the material decomposition task. An average accuracy of 0.9% for $\rho_e$ and 1% for $Z_{eff}$ is comparable to our method, but the dose level used was not reported. The analysis was performed on low-$Z_{eff}$ plastic materials using a pair of monochromatic acquisitions. Considerably more papers using conventional systems have been published, but not focusing on breast tissues or breast dedicated scanners. Szczykutowicz *et al* (2011) performed a methodologically similar approach to the one presented in this paper using a clinical scanner and test object without any noise remedying approach. They successfully decompose electron density and $Z_{eff}$ but at the cost of a significant reduction in signal-to-noise ratio. Lalonde and Bouchard (2016) developed a model in which materials are decomposed in a compressed basis with principal component analysis, using the fact that human tissues are composed of a very limited number of elements. Then, the first principal components are virtual materials containing a certain fraction of those elements. From there $Z_{eff}$ values were computed. Azevedo *et al* (2016) implemented their System-Independent-Rho-Z (SIRZ) method to obtain physical quantities of phantom materials independent of the shape of the X-ray spectrum. The photoelectric-Compton decomposition is performed in sinogram space and absolute $\rho_e$ and $Z$ values are obtained after the calibration procedure. While physical characterization was successfully described for materials of fairly distinguishable compositions, the noise behavior was also not described in this work. Champley *et al* (2019) released a follow-up paper focusing on the optimization and simplification of spectral modeling as a new method called SIRZ-2. Most recently, Busi *et al* (2019) developed a physical characterization method using spectral detectors. They claim higher robustness and increased estimation accuracy (25%) compared to SIRZ methods. Extended work from the same group was published in Jumanazarov *et al* (2021) to optimize the computation speed. Machine learning solutions to $\rho/Z_{eff}$ extraction were also tested by Su *et al* (2018) using dedicated phantoms with several tissue-equivalent inserts. Good results in computing $Z_{eff}$ were obtained using artificial neural networks and the random forest method with a relative error between 1% and 2% at clinically relevant doses. However, a low-dose scanning and evaluation of the model on materials that were removed from the training set led to errors of up to 6%. Nonetheless, the authors showed that the machine learning approach is robust and computationally efficient.

Considering specifically the estimation of $\rho$ and $Z_{eff}$ for breast tissues, only a few studies exist and most have been made with experimental setups not used in diagnostic radiology. Berggren *et al* (2018) performed clinical evaluation of breast skin $Z_{eff}$ obtained from 709 screening patients using planar spectral mammography. They reported slightly higher values of 7.365 (95% confidence interval: 7.364, 7.366) comparable to our findings of $7.31 \pm 0.06$, with a difference of less than 1% that might be due to the fact that tissues in our experiment were formalin-fixed. Gobo *et al* (2020) used a combination of transmission and scattering measurements with $^{241}$Am source and an x-ray tube, while Antoniassi *et al* (2011) performed scattering measurements at 90 degrees by using low-energy beams. Given diverse formulations of $Z_{eff}$ across the literature, we made a comparison in relative change using $Z_{eff}$ of nylon as a reference value in table 4.

Our study shows potential for quantitative breast imaging by translating spectral information into the computation of physically relevant quantities, but it also has some limitations. The accuracy of the presented method is mainly governed by the quality of material decomposition, which is highly dependent on the denoising of decomposed data. We gave up the spatial information inside the ROI to obtain quantitatively correct material decomposition during the 2D Gaussian denoising approach. Inaccurate tissue segmentation would result in an erroneous Gaussian fitting procedure as the number of peaks in 2D histogram space

**Table 4.** Literature review of experimentally obtained density and $Z_{eff}$ numbers for fibro-glandular, adipose and tumorous tissues.

| Tissue type | Density $\rho$ | | $Z_{eff}$ to nylon % diff | | |
|---|---|---|---|---|---|
| | This work | Gobo *et al* | This work | Gobo *et al* | Antoniassi *et al* |
| Fibro-glandular | 0.96 | 1.04 | 15.38 | 16.73 | 14.07 |
| Adipose | 0.90 | 0.95 | 2.68 | 4.40 | 5.60 |
| Tumorous | 1.07 | 1.05 | 21.31 | 18.87 | 14.79 |

corresponds to the number of tissue types being evaluated at once. The appearance of a histogram containing several plastic materials was published in our previous study (Vrbaski *et al* 2021). Thus, either correct tissue segmentation or an algorithm capable of correctly fitting multiple Gaussian functions in case no segmentation is performed are critical aspects of the present model. For the proof of concept, we relied on high-quality synchrotron beam radiation, but to make this approach broadly used, we plan to apply the method to more accessible polychromatic sources. Finally, the conclusions drawn in this study were based on the analysis of 5 mastectomy samples fixed in formalin which could slightly bias the measured $\mu$ values (less than 0.5% (Fredenberg *et al* 2018)). More samples will be evaluated to further confirm these findings. Despite the mentioned limitations, given the general validity of the proposed decomposition model and the foreseeable use of spectral detectors in breast CT scanners, the present feasibility study paves the way for its application to clinical spectral breast CT data.

## 5. Conclusions

A model incorporating CT reconstructions of an arbitrary number of spectral energy channels was developed to compute material density and effective atomic number. The density and effective atomic number of soft-tissue-equivalent plastic materials were computed with an average accuracy in the order of 1%, and the same approach was applied to the set of 5 mastectomy samples. The quantitative analysis presented here suggests that adipose, fibro-glandular, and tumorous tissues can be distinguished, given the MSSs obtained for each tissue pair. Density and effective atomic number can also be used for physics-based extrapolation of virtual monochromatic linear attenuation coefficients outside of the experimental energy range. Breast CT is an emerging technology that is capable to provide three-dimensional imaging of the breast and its extension to spectral imaging is certainly desirable for exploring the potential of material characterization in clinical trials.

## Acknowledgments

## Data availability statement

All data that support the findings of this study are included within the article (and any supplementary information files). Data will be available from 1 June 2023.

## Appendix A. Noise analysis and uncertainties

As it was shown in section 2.5, regions of uniform composition result in scattered values of elongated shape (i.e. clusters) in the $(x_1, x_2)$-plane histogram. Such behavior was ascribed to the unavoidable amount of noise carried by the tomographic reconstructions on which the whole decomposition method is based. Detailed analysis of the propagation of measurement uncertainties, related to the size of the cluster, was carried out. The Gaussian fitting procedure introduced in section 2.5 individuates a preferred direction at angle $\theta$ aligned to the major axis $u$ of elliptical Gaussian. The length in this direction and the orthogonal one (minor axis) are identified as the

Gaussian spreads in a reference frame $(x_u, x_v)$, which is parallel to the major and minor axes of the spot. The standard errors of the centroid coordinates can be approximated by the ratios between the Gaussian spreads $S_u$ and $S_v$ and the square root of the volume under the Gaussian surface

$$\sigma_{x_u} = \frac{S_u}{\sqrt{V}}, \tag{1.1a}$$

$$\sigma_{x_v} = \frac{S_v}{\sqrt{V}}, \tag{1.1b}$$

where the volume is given as

$$V = 2\pi\, A\, \frac{S_u\, S_v}{b_1\, b_2} \tag{1.2}$$

that it is equal to the total number of voxels contributing to the corresponding two-dimensional Gaussian function. Quantities $b_1$ and $b_2$ are bin sizes in both directions and $A$ is the peak value. Calculated errors are then translated into uncertainties of coordinates $x_\xi$ and $x_\zeta$ in the reference frame rotated by the angle $\phi$ defined in section 2.1. Rotation from the frame identified by angle $\theta$ to the frame identified by angle $\phi$ is defined as

$$\begin{bmatrix} x_\xi \\ x_\zeta \end{bmatrix} = \begin{bmatrix} \cos\alpha & \sin\alpha \\ -\sin\alpha & \cos\alpha \end{bmatrix} \begin{bmatrix} x_u \\ x_v \end{bmatrix},$$

where $\alpha = \phi - \theta$. Propagating uncertainty through the rotation of the reference frame leads to

$$\sigma^2_{x_\xi} = \cos^2\alpha\, \sigma^2_{x_u} + \sin^2\alpha\, \sigma^2_{x_v}, \tag{1.3a}$$

$$\sigma^2_{x_\zeta} = \sin^2\alpha\, \sigma^2_{x_u} + \cos^2\alpha\, \sigma^2_{x_v}. \tag{1.3b}$$

From the rotated frame, to the rescaled $x_\rho, x_Z$ frame, the division of the second coordinate by the first one implicates

$$\sigma^2_{x_Z} = \frac{x_\zeta^2}{x_\xi^4}\sigma^2_{x_\xi} + \frac{1}{x_\xi^2}\sigma^2_{x_\zeta} \tag{1.4}$$

while propagating $x_\rho$ remains trivial

$$\sigma^2_{x_\rho} = \sigma^2_{x_1}. \tag{1.5}$$

Finally, shifting to the pair $\rho, Z$ requires equations (6a) and (6b), leading to the uncertainties

$$\sigma_\rho = \kappa^{-1}\, \sigma_{x_\rho} \tag{1.6a}$$

$$\sigma_Z = \frac{(x_Z - q)^{\frac{1-\lambda}{\lambda}}}{\lambda\, p^{1/\lambda}}\, \sigma_{x_Z}. \tag{1.6b}$$

## Appendix B. Noise behavior in 2D histogram space

In addition to the estimated centers of the distributions in figure 3(a), the 2D Gaussian fit method outputs several other parameters relevant for the accurate estimation of basis material concentrations summarized in

**Table B1.** List of output parameters in 2D Gaussian fitting method for the phantom materials.

| Material | Amplitude $(A)$ | Major axis spread $S_u$ | Minor axis spread $S_v$ | Angle $\theta$ |
|---|---|---|---|---|
| Water | 38 | 0.40 | 0.0074 | −0.121 |
| PE | 40 | 0.37 | 0.0065 | −0.121 |
| PA | 38 | 0.32 | 0.0062 | −0.120 |
| PMMA | 38 | 0.41 | 0.0073 | −0.121 |
| POM | 38 | 0.32 | 0.0062 | −0.120 |
| PTFE | 41 | 0.46 | 0.0078 | −0.121 |

table B1. The angle $\theta$ at which the cluster is extended remains constant ($\simeq -0.12$) for all materials indicating that blurring is not dependent on the material type. It is rather a result of combined contributions of image acquisition, reconstruction, and material decomposition noise. The amount of blurring in the major direction $S_u$ and the direction orthogonal to it $S_v$ is of the same order of magnitude for all materials. The $S_u$ values are around 2 orders of magnitude larger than $S_v$ values. The amplitude $A$ of the Gaussian function remains constant for the same size of the ROI for all plastic inserts. These properties are important for the Gaussian fitting procedure because an initial guess for fitting parameters can be given, improving the robustness of the method and increasing the computational speed. A more rigorous statistical description of these features will be the subject of a forthcoming standalone communication.

## Appendix C. Comparison of methods used to compute the atomic number of a compound —Z*comp*ARE

Effective atomic number as a property of a material depends on its chemical composition, but it is not uniquely defined in the literature. Very often different definitions are adopted by researchers depending on the experimental setup, energy range, and type of compounds. Several definitions that have been proposed to compute this quantity can be divided into: (i) methods that compute $Z_{eff}$ as a weighted average of composing elements in the compound, (ii) and methods that rely on mass attenuation coefficients of composing elements to compute $Z_{eff}$ (Bonnin *et al* 2014). The second group of methods was developed to solve the fundamental problem: $Z_{eff}$ as the quantity defined in the first category is not specifically tied to the absorption property of a material. Thus, weighted sums of elements in a compound used in the first category are exclusively valid for certain energy ranges and often to a certain set of elements contained in the mixture, while methods in the second category rely on tabulated attenuation properties of materials to inherently define $Z_{eff}$ as a quantity tied to attenuation property of the material.
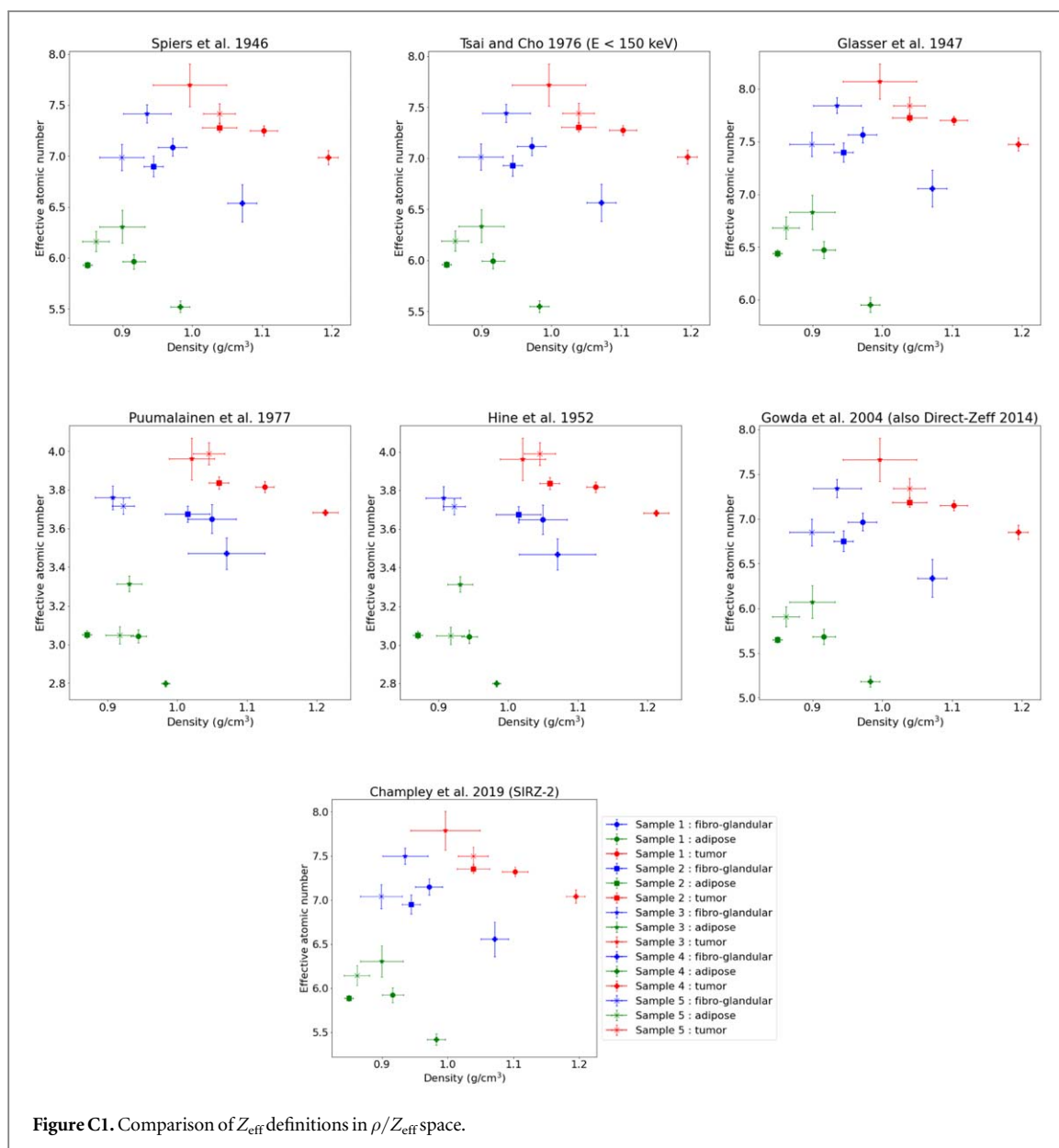
In this section, we compared several available methods for the materials in the calibration phantom. Z*comp*ARE (Vrbaski 2022) is user-friendly software with a graphical interface that can be used to compare several methods most often used. The comparison of the methods for the calibration phantom materials in the energy range 20–40 keV is given in table C1.

It can be seen that methods by Spiers *et al*, Tsai and Cho, Glasser *et al*, Gowda *et al*, and Champley *et al* provide very similar $Z_{eff}$ numbers for our experimental conditions. Methods by Hine *et al* and Puumalainen *et al* gave considerably lower $Z_{eff}$ numbers for all materials. Calibration functions of the form defined in equations (6*a*) and (6*b*) were applied to all definitions for $Z_{eff}$ and results are given in figure C1. The MSS defines the level of separation in the range $-1$ to 1 was found to be approx. 0.31 for all methods used. Thus, the distinguishment of tissues could be obtained irrespective of the proposed definition.

The method defined by Champley *et al* (2019) showed slightly better agreement of virtual monochromatic $\mu$ values computed using equation (3) with experimentally measured data. Constants $n$, $K_1$, and $K_2$ used in equation (3) were estimated to be 4.44, 9.4, and 1.6 using the least-square fit method for elemental materials found in the human body in the $Z$ range of 1–20 across the diagnostic energy range (20–200 keV).

**Table C1.** Comparison of the most often used formulations of effective atomic numbers for phantom materials in the energy range 20–40 keV.

| Material | Water | PE | PA | PMMA | POM | PTFE |
|---|---|---|---|---|---|---|
| Brute formula | $H_2O$ | $C_2H_4$ | $C_{12}H_{22}N_2O_2$ | $C_5H_8O_2$ | $CH_2O$ | $C_2F_4$ |
| Spiers *et al* | 7.42 | 5.44 | 6.12 | 6.47 | 6.95 | 8.43 |
| Glasser *et al* | 7.96 | 5.94 | 6.60 | 6.94 | 7.38 | 8.62 |
| Hine *et al* | 3.34 | 2.67 | 3.27 | 3.60 | 4.00 | 7.99 |
| Puumalainen *et al* | 3.33 | 2.67 | 3.27 | 3.61 | 4.00 | 8.00 |
| Tsai and Cho | 7.44 | 5.47 | 6.15 | 6.50 | 6.98 | 8.45 |
| Gowda *et al* | 7.24 | 5.05 | 5.89 | 6.32 | 6.85 | 8.53 |
| Champley *et al* | 7.44 | 5.28 | 6.16 | 6.49 | 7.01 | 8.56 |

**Figure C1.** Comparison of $Z_{\mathrm{eff}}$ definitions in $\rho/Z_{\mathrm{eff}}$ space.

## ORCID iDs

Stevan Vrbaški ⓘ https://orcid.org/0000-0003-3722-7447

Lucia Mariel Arana Peña ⓘ https://orcid.org/0000-0001-5998-9499

Luca Brombal ⓘ https://orcid.org/0000-0002-4009-8191

Sandro Donato ⓘ https://orcid.org/0000-0003-0696-9077

Angelo Taibi ⓘ https://orcid.org/0000-0002-2494-8993

Adriano Contillo ⓘ https://orcid.org/0000-0001-6563-2330

Renata Longo ⓘ https://orcid.org/0000-0002-7782-9218

## References

Albrecht M H *et al* 2019 Review of clinical applications for virtual monoenergetic dual-energy CT *Radiology* **293** 260–71

Alvarez R E and Macovski A 1976 Energy-selective reconstructions in x-ray computerised tomography *Phys. Med. Biol.* **21** 733–44

Antoniassi M, Conceição A L C and Poletti M E 2011 Study of effective atomic number of breast tissues determined using the elastic to inelastic scattering ratio *Nucl. Instrum. Methods Phys. Res.* A **652** 739–43

Azevedo S G, Martz H E, Aufderheide M B, Brown W D, Champley K M, Kallman J S, Roberson G P, Schneberk D, Seetho I M and Smith J A 2016 System-independent characterization of materials using dual-energy computed tomography *IEEE Trans. Nucl. Sci.* **63** 341–50

Bellazzini R, Spandre G, Brez A, Minuti M, Pinchera M and Mozzo P 2013 Chromatic X-ray Imaging with A Fine Pitch CdTe Sensor Coupled to A Large Area Photon Counting Pixel ASIC *Journal of Instrumentation* **8** C02028

Berger N, Marcon M, Saltybaeva N, Kalender W A, Alkadhi H, Frauenfelder T and Boss A 2019 Dedicated breast computed tomography with a photon-counting detector: initial results of clinical in vivo imaging *Investigative Radiol.* **54** 409–18

Berggren K, Eriksson M, Hall P, Wallis M G and Fredenberg E 2018 In vivo measurement of the effective atomic number of breast skin using spectral mammography *Phys. Med. Biol.* **63** 215023

Bonnin A, Duvauchelle P, Kaftandjian V and Ponard P 2014 Concept of effective atomic number and effective mass density in dual-energy X-ray computed tomography *Nucl. Instrum. Methods Phys. Res.* B **318** 223–31

Brombal L, Donato S, Brun F, Delogu P, Fanti V, Oliva P, Rigon L, Di Trapani V, Longo R and Golosio B 2018a Large-area single-photon-counting CdTe detector for synchrotron radiation computed tomography: a dedicated pre-processing procedure *J. Synchrotron Radiat.* **25** 1068–77

Brombal L *et al* 2018b Phase-contrast breast CT: the effect of propagation distance *Phys. Med. Biol.* **63** 24NT03

Brun F, Massimi L, Fratini M, Dreossi D, Billè F, Accardo A, Pugliese R and Cedola A 2017 SYRMEP tomo project: a graphical user interface for customizing CT reconstruction workflows *Adv. Struct. Chem. Imaging* **3** 1–9

Brunetti A, Sanchez del Rio M, Golosio B, Simionovici A and Somogyi A 2004 A library for X-ray-matter interaction cross sections for X-ray fluorescence applications *Spectrochim. Acta* B **59** 1725–31

Busi M, Kehres J, Khalil M and Olsen U L 2019 Effective atomic number and electron density determination using spectral x-ray CT *Proc SPIE* **10999** 1099903

Champley K M, Azevedo S G, Seetho I M, Glenn S M, McMichael L D, Smith J A, Kallman J S, Brown W D and Martz H E 2019 Method to extract system-independent material properties from dual-energy x-ray CT *IEEE Trans. Nucl. Sci.* **66** 674–86

Chen R C *et al* 2010 Measurement of the linear attenuation coefficients of breast tissues by synchrotron radiation computed tomography *Phys. Med. Biol.* **55** 499317

Contillo A, Veronese A, Brombal L, Donato S, Rigon L, Taibi A, Tromba G, Longo R and Arfelli F 2018 A proposal for a quality control protocol in breast ct with synchrotron radiation *Radiol. Oncol.* **52** 329–36

Danielsson M, Persson M and Sjölin M 2021 Photon-counting x-ray detectors for CT *Phys. Med. Biol.* **66** 03TR01

Delogu P, Oliva P, Bellazzini R, Brez A, Ruvo P L d, Minuti M, Pinchera M, Spandre G and Vincenzi A 2016 Characterization of Pixirad-1 photon counting detector for x-ray imaging **11** P01015

Donato S *et al* 2022 Optimization of a customized simultaneous algebraic reconstruction technique algorithm for phase-contrast breast computed tomography *Phys. Med. Biol.* **67** 095012

Dong X, Niu T and Zhu L 2014 Combined iterative reconstruction and image-domain decomposition for dual energy CT using total-variation regularization *Med. Phys.* **41** 051909

Fedon C, Longo F, Mettivier G and Longo R 2015 GEANT4 for breast dosimetry: parameters optimization study **60** N311–23

Fredenberg E, Willsher P, Moa E, Dance D R, Young K C and Wallis M G 2018 Measurement of breast-tissue x-ray attenuation by spectral imaging: fresh and fixed normal and malignant tissue *Phys. Med. Biol.* **63** 235003

Gobo M S S, Soares L D H and Poletti M E 2020 Effective atomic number of breast tissues determined by transmission and scattering methods *Radiat. Phys. Chem.* **167** 108260

Gureyev T E, Nesterets Y I, Kozlov A, Paganin D M and Quiney H M 2017 On the unreasonable effectiveness of transport of intensity imaging and optical deconvolution *J. Opt. Soc. Am.* A **34** 2251–60

Heismann B J, Leppert J and Stierstorfer K 2003 Density and atomic number measurements with spectral x-ray attenuation method *J. Appl. Phys.* **94** 2073–9

Hudobivnik N *et al* 2016 Comparison of proton therapy treatment planning for head tumors with a pencil beam algorithm on dual and single energy CT images *Med. Phys.* **43** 495–504

Jumanazarov D, Koo J-K, Poulsen H F, Olsen U L and Iovea M 2021 The significance of the spectral correction of photon counting detector response in material classification from spectral x-ray CT *Quantum Optics and Photon Counting 2021 SPIE* ed I Prochazka *et al* (Czech Republic: SPIE) p 15

Kalender W A, Kolditz D, Steiding C, Ruth V, Lück F, Röler A-C and Wenkel E 2017 Technical feasibility proof for high-resolution low-dose photon-counting CT of the breast *Eur. Radiol.* **27** 1081–6

Lalonde A and Bouchard H 2016 A general method to derive tissue parameters for Monte Carlo dose calculation with multi-energy CT *Phys. Med. Biol.* **61** 8044–69

Lehmann L A, Alvarez R E, Macovski A, Brody W R, Pelc N J, Riederer S J and Hall A L 1981 Generalized image combinations in dual KVP digital radiography *Med. Phys.* **8** 659–67

Liu L P, Hwang M, Hung M, Soulen M C, Schaer T P, Shapira N and Noël P B 2023 Non-invasive mass and temperature quantifications with spectral CT *Sci. Rep.* **13** 61091

Longo R *et al* 2016 Towards breast tomography with synchrotron radiation at Elettra: first images *Phys. Med. Biol.* **61** 1634–49

Longo R *et al* 2019 Advancements towards the implementation of clinical phase-contrast breast computed tomography at Elettra *J. Synchrotron Radiat.* **26** 1343–53

McCollough C H, Leng S, Yu L and Fletcher J G 2015 Dual- and multi-energy ct: principles, technical approaches, and clinical applications *Radiology* **276** 637–53

Mechlem K, Allner S, Mei K, Pfeiffer F and Noël P B 2016 Dictionary-based image denoising for dual energy computed tomography *Proc SPIE* **9783** 97830E

Mettivier G, Fedon C, Di Lillo F, Longo R, Sarno A, Tromba G and Russo P 2016 Glandular dose in breast computed tomography with synchrotron radiation *Phys. Med. Biol.* **61** 569–87

Niu T, Dong X, Petrongolo M and Zhu L 2014 TU-F-18A-02: iterative image-domain decomposition for dual-energy CT *Med. Phys.* **41** 475–6

Paganin D, Mayo S C, Gureyev T E, Miller P R and Wilkins S W 2002 Simultaneous phase and amplitude extraction from a single defocused image of a homogeneous object *J. Microsc.* **206** 33–40

Pascart T, Norberciak L, Legrand J, Becce F and Budzik J F 2019 Dual-energy computed tomography in calcium pyrophosphate deposition: initial clinical experience *Osteoarthritis Cartilage* **27** 1309–14

Piai A *et al* 2019 Quantitative characterization of breast tissues with dedicated CT imaging *Phys. Med. Biol.* **64** 155011

Puumalainen P, Olkkonen H and Sikanen P 1977 Assessment of fat content of liver by a photon scattering technique *Int. J. Appl. Radiat. Isotopes* **28** 785–7

Rajendran K *et al* 2021 First clinical photon-counting detector ct system: technical evaluation *Radiol.* **303** 130–8

Rajiah P, Parakh A, Kay F, Baruah D, Kambadakone A R and Leng S 2020 Update on multienergy CT: physics, principles, and applications *RadioGraphics* **40** 1284–308

Rousseeuw P J 1987 Silhouettes: a graphical aid to the interpretation and validation of cluster analysis *J. Comput. Appl. Math.* **20** 53–65

Schmidt C S, Zellweger C, Wieler J, Berger N, Marcon M, Frauenfelder T and Boss A 2022 Clinical assessment of image quality, usability and patient comfort in dedicated spiral breast computed tomography *Clin. Imaging* **90** 50–8

Schoonjans T, Brunetti A, Golosio B, del Rio M S, Sole V A, Ferrero C and Vincze L 2011 The xraylib library for x-ray-matter interactions: recent developments *Spectrochim. Acta* B **66** 776–84

Spiers F W 1946 Effective atomic number and energy absorption in tissues *Br. J. Radiol.* **19** 52–63

Su K-H *et al* 2018 Machine learning-based dual-energy CT parametric mapping *Phys. Med. Biol.* **63** 125001

Szczykutowicz T P, Qi Z and Chen G-H 2011 A simple image based method for obtaining electron density and atomic number in dual energy CT *Medical Imaging 2011: Physics of Medical Imaging SPIE* ed N J Pelc *et al* (Florida: Lake Buena Vista) p 79613A

Tavakoli Taba S *et al* 2021 Propagation-based phase-contrast ct of the breast demonstrates higher quality than conventional absorption-based ct even at lower radiation dose *Acad. Radiol.* **28** e20–6

Torikoshi M, Tsunoo T, Sasaki M, Endo M, Noda Y, Ohno Y, Kohno T, Hyodo K, Uesugi K and Yagi N 2003 Electron density measurement with dual-energy x-ray CT using synchrotron radiation *Phys. Med. Biol.* **48** 673–85

Tsai C M and Cho Z H 1976 Physics of contrast mechanism and averaging effect of linear attenuation coefficients in a computerized transverse axial tomography (CTAT) transmission scanner *Phys. Med. Biol.* **21** 544

Un A and Caner T 2014 The direct-zeff software for direct calculation of mass attenuation coefficient, effective atomic number and effective electron number *Ann. Nucl. Energy* **65** 158–65

Vrbaski S 2022 ZcompARE. original-date: 2022-11-17T15:56:00Z

Vrbaski S, Longo R and Contillo A 2022 From Spectral Decomposition through SVD to Quantitative Description of Monochromatic CT images: a Phantom Study *Proc SPIE* **12031** 1203132

Vrbaski S, Longo R, Taibi A and Contillo A 2021 Quantitative material characterization based on the spectral decomposition of X-ray tomographic images *Il Nuovo Cimento* C **44** 144

Zellweger C, Berger N, Wieler J, Cioni D, Neri E, Boss A, Frauenfelder T and Marcon M 2022 Breast computed tomography: diagnostic performance of the maximum intensity projection reformations as a stand-alone method for the detection and characterization of breast findings *Investigative Radiol.* **57** 205–11

Zhang W, Zhang H, Wang L, Wang X, Cai A, Li L, Niu T and Yan B 2019 Image domain dual material decomposition for dual-energy CT using butterfly network *Med. Phys.* **46** 2037–51